Research in Astronomy and Astrophysics, 24:065019 (11pp), 2024 June https://doi.org/10.1088/1674-4527/ad4598

Feedback of Efficient Shock Acceleration on Magnetic-field Structure Inside Young Type Ia Supernova Remnants

Jun-Yu Shen[1], Bi-Wen Bao[1,2], and Li Zhang[1]

[1] Department of Astronomy, Key Laboratory of Astroparticle Physics of Yunnan Province, Yunnan University, Kunming 650091, China; baobiwen@ynu.edu.cn, lizhang@ynu.edu.cn

[2] Key Laboratory of Statistical Modeling and Data Analysis of Yunnan Province, Yunnan University, Kunming 650091, China

Received 2024 January 3; revised 2024 March 26; accepted 2024 April 19; published 2024 June 7

Abstract

Using an effective adiabatic index $\gamma_{\rm eff}$ to mimic the feedback of efficient shock acceleration, we simulate the temporal evolution of a young type Ia supernova remnant (SNR) with two different background magnetic field (BMF) topologies: a uniform and a turbulent BMF. The density distribution and magnetic-field characteristics of our benchmark SNR are studied with two-dimensional cylindrical magnetohydrodynamic simulations. When $\gamma_{\rm eff}$ is considered, we find that: (1) the two-shock structure shrinks and the downstream magnetic-field orientation is dominated by the Rayleigh–Taylor instability structures; (2) there exists more quasi-radial magnetic fields inside the shocked region; and (3) inside the intershock region, both the quasi-radial magnetic energy density and the total magnetic energy density are enhanced: in the radial direction, with $\gamma_{\rm eff} = 1.1$, they are amplified about 10–26 times more than those with $\gamma_{\rm eff} = 5/3$. While in the angular direction, the total magnetic energy densities could be amplified about 350 times more than those with $\gamma_{\rm eff} = 5/3$, and there are more grid cells within the intershock region where the magnetic energy density is amplified by a factor greater than 100.

Key words: methods: numerical – ISM: magnetic fields – ISM: supernova remnants – magnetohydrodynamics (MHD)

1. Introduction

Supernova remnants (SNRs) arise from the interactions of expanding ejecta with the interstellar medium (ISM), giving rise to a two-shock structure susceptible to hydrodynamical instabilities (McKee & Truelove 1995; Wang & Chevalier 2001). This specific structure includes a forward shock (FS) compressing and heating the ISM, a reverse shock (RS) generated by supersonic collisions between the outermost ejecta and the shell (McKee 1974), and contact discontinuity (CD). The CD is an interface where Rayleigh–Taylor instability (RTI) occurs due to a density discontinuity between the shocked ISM and shocked ejecta (Reynolds 2017; Zhou 2017a, 2017b). Specifically, finger-like structures will appear and grow in the hydrodynamical unstable region, as the shocked ejecta permeates into the shocked ISM. Besides, due to the tangential velocity disparity between the shocked ISM and shocked ejecta, the secondary Kelvin–Helmholtz instability (KHI) could emerge at the tips of the finger-like structures (Jun et al. 1996).

As revealed by observations and numerical simulations, the two-shock structure plays a crucial role in the evolution of an SNR and the particle acceleration process: the strong forward shock will compress the background magnetic field (BMF) perpendicular to its normal direction (Vink 2020), thereby increasing the tangential component of the magnetic field in the downstream. Then the RTI can further amplify the swept-up magnetic field greatly. Since the magnetic-field lines are frozen in the plasma, they could be strongly stretched and distorted by the RTI and the velocity-sheared vortices caused by the KHI behind the mushroom caps (Jun et al. 1996). Therefore, the finger-like structures exert an obvious amplification effect on the downstream magnetic field (Jun & Norman 1996a), leading to a radial predominance of the magnetic-field orientation in the main shell of young SNRs (Jun & Norman 1996b). Based on observational data, the postshock magnetic field in SNRs can reach $\sim 10^{-4}$ G, much higher than the results from simple shock compression. Notable examples include the Tycho SNR (Völk et al. 2005; Warren et al. 2005) and the Cassiopeia A (Vink & Laming 2003), providing strong indications for the contributions of RTI to the magnetic-field amplification (MFA).

Furthermore, it is theoretically predicted that MFA would occur during the evolution of SNRs, manifesting itself in an amplified magnetic field δB much larger than the pre-existing ordered magnetic field B_0, i.e., $\delta B/B_0 \gg 1$. Apart from RTI, MFA could be attributed to multiple physical mechanisms, including resonant cosmic ray (CR) streaming instability (Bell 1978; Zweibel 1979; Schure et al. 2012), Bell instability (Bell 2004, 2013; Blasi 2013), and turbulent dynamo (Giacalone & Jokipii 2007; Xu & Lazarian 2016; Hu et al. 2022). Since the magnetic field is dynamically important in the SNR lifetime, especially the post-adiabatic epochs (Petruk et al. 2016, 2018, 2021), magnetic energy density could be a relevant physical quantity worthy of research. The temporal evolution of magnetic energy density in SNRs has been studied by several papers via numerical simulations (Jun & Norman 1996a, 1996b; Jun & Jones 1999; Shin et al. 2008). Note that magnetic energy density is expressed as $B^2/8\pi$, the ratio $\delta B^2/B_0^2$ could be used to characterize the MFA in simulations and assess the amplification efficiency (Lucek & Bell 2000; Riquelme & Spitkovsky 2009).

SNRs are generally regarded as one of the main sources of Galactic CRs below the "knee" energy ($E \approx 3 \times 10^{15}$ eV) (Baade & Zwicky 1934; Reynolds 2008). The mechanism of accelerating CRs to such high energy is considered to be the nonlinear diffusive shock acceleration (DSA) (see, e.g., Blasi 2013; Amato 2014). Recent observations in both the TeV and GeV bands have collected a great deal of data concerning specific SNRs, such as SN 1006 (Acero et al. 2010), Tycho SNR (Acciari et al. 2011), W44 (Cardillo et al. 2014), and HESS J1731-347 (Yang et al. 2014), which further confirmed that SNRs are indeed important particle acceleration sites. In numerical simulations, an effective adiabatic index $\gamma_{\rm eff}$ is adopted to mimic the feedback of the efficient shock acceleration process (Chevalier 1983; Decourchelle et al. 2000; Fraschetti et al. 2010; Wang 2011; Orlando et al. 2012).

Regarding the particle acceleration process, a growing body of evidence proves that it is linked with the two-shock structure (Reynolds 2008; Telezhinsky et al. 2013). When the efficient shock acceleration occurs, the impacts of relativistic particles on pressure and the escape of superthermal particles result in an effective adiabatic index $\gamma_{\rm eff}$ less than $5/3$ (Blondin & Ellison 2001; Fraschetti et al. 2010; Wang 2011; Orlando et al. 2012). This could increase the compression ratio of the shock, leading to further compression of the BMF in the downstream (Schure et al. 2012). Besides, the CR acceleration process is also constrained by the magnetic-field structure in situ. For example, the angle between the shock normal and the magnetic field can affect the particle acceleration efficiency (Reynoso et al. 2013; West et al. 2016). Moreover, the SNR expanding in a non-uniform magnetized background would enhance the turbulence in the postshock region, in turn impacting on the acceleration process (Balsara et al. 2001). The above two factors alter the energy transfer process during the acceleration by influencing the scattering efficiency (Xu & Lazarian 2022).

Results from earlier research indicate the existence of magnetic fields with different topologies in space: ordered fields in galaxies (Beck 2016; Han 2017), turbulent fields around type Ia SNRs (Shimoda et al. 2018; Saha et al. 2019), radial and toroidal fields generated by progenitor stellar winds (Parker 1958). These diverse BMFs could serve as the pre-SN environment. Regarding various pre-SN magnetic-field topologies in the ambient medium, the FS could compress the magnetic field to varying degrees in all directions. Thus, the magnetic-field structure inside the shocked region might be different.

Given their specific ejecta mass and dynamical properties, Type Ia SNRs, relics of thermonuclear explosions in binary systems, are considered the ideal objects to study the evolution of SNRs (Lopez et al. 2011). For this reason, numerous investigations have been done in recent studies, concerning the dynamical processes and the morphologies of type Ia SNRs: the multiband-emission morphologies of SNRs under diverse BMFs (Orlando et al. 2007, 2011; Bao et al. 2018; Zhang et al. 2023); the magnetic-field evolution of the SNR in a turbulent BMF (Guo et al. 2012; Peng et al. 2020; Bao et al. 2021); the feedback of the particle acceleration processes on the SNR temporal evolution (Ferrand et al. 2010; Jun & Li 2012). Besides, some radio-polarization measurements inform us about the overall magnetic-field orientation in type Ia SNRs. For mature SNRs, the polarization vectors are mostly consistent with a tangentially oriented magnetic field due to shock compression (Dickel & Milne 1976). In contrast, radially oriented magnetic fields are observed in many young type Ia SNRs, such as Tycho (Reynoso et al. 1997), Kepler (DeLaney et al. 2002), and SN 1006 (Reynoso et al. 2013). With respect to the origin of the radial component, it is generally assumed that RTI will stretch the field lines preferentially along the radial direction (Gull & Longair 1973; Jun & Norman 1996b; Dubner & Giacani 2015). If there exists density inhomogeneities in the ejecta, the RT fingers will approach the FS (Orlando et al. 2012, 2019). Meanwhile, turbulence driven by Richtmyer–Meshkov instability at the tips of the fingers could also result in amplification of the radial component of magnetic fields (Inoue et al. 2013). These processes may explain the radial orientation preference observed in young SNRs. Despite that, efficient shock acceleration could modify the magnetic-field structure in a type Ia SNR, its potential impacts on the distribution of magnetic-field orientation and magnetic energy density, as well as the amplification of magnetic energy density within the main shell have not yet been assessed.

In this paper, by adopting $\gamma_{\rm eff}$ to mimic the feedback of efficient shock acceleration, we make an attempt to investigate the downstream magnetic-field structure of a young type Ia SNR. Considering two different BMF topologies, namely a uniform and a turbulent BMF, we explore the magnetic-field orientation and the magnetic-field energy density within our benchmark SNR via 2D cylindrical magnetohydrodynamics (MHD) simulations. The sketch of this paper is as follows. In Section 2, a detailed description of the initial setups for our numerical simulations is given. The density distribution and magnetic field characteristics are presented in Section 3. We give some conclusions and discussion in Section 4.

2. Simulation Description

2.1. Initial Density Profiles of a Type Ia SNR

It is proposed by Chevalier (1982) to use the power-law profile to describe a type Ia SNR after the explosion. This model assumes that the mass density in the ejecta and circumstellar medium of the SNR can be described by a power law, providing a spherically symmetric and self-similar solution for the ejecta-dominated SNR structure (Blondin & Ellison 2001). Since the steep power-law density distribution of the ejecta will lead to an infinite ejecta mass, the ejecta density profile should be truncated at a small radius r_c, where $r_c = v_c t$. When the radius is less than r_c, the ejecta density is assumed to be a constant value, and 4/7 of the total mass is contained in this inner plateau. When the radius is greater than r_c, the ejecta density is distributed according to a given power law, and 3/7 of the total mass is contained in the outer part:

$$\rho_{\rm ej}(r, t) = \begin{cases} \rho_c v_c^n r^{-n} t^{n-3} & \text{for } r > v_c t, \\ \rho_c t^{-3} & \text{for } r < v_c t, \end{cases} \tag{1}$$

where t is the age since the supernova explosion and $n = 7$ is adopted for type Ia SNRs. The expression of constant ρ_c is[3]:

$$\rho_c = \frac{5n - 25}{2\pi n} E_{\rm ej} v_c^{-5}, \tag{2}$$

where v_c is the velocity of matter at r_c and given by:

$$v_c = \left(\frac{10n - 50}{3n - 9} \frac{E_{\rm ej}}{M_{\rm ej}}\right)^{1/2}. \tag{3}$$

Here, we adopt $E_{\rm ej} = 1.0 \times 10^{51}$ erg for the total kinetic energy of the ejecta and $M_{\rm ej} = 1.4\,M_\odot$ for the ejecta mass, respectively. The initial radius of the ejecta $R_{\rm ej}$ is 0.5 pc, corresponding to an initial age of about 9 yr (Dwarkadas & Chevalier 1998).[4] We take the background temperature T_0 to be 10^4 K and the background density $\rho_{\rm ISM}$ to be $0.1\ {\rm cm}^{-3}$, respectively. Throughout this paper, the mass density is in units of $m_{\rm H}$ ${\rm cm}^{-3}$ ($m_{\rm H}$ is the mass of a hydrogen atom), while the magnetic field is in units of μG. All other physical quantities are expressed in c.g.s. units.

2.2. MHD Simulation Settings

The ideal MHD equations including mass conservation equation, momentum conservation equation, energy conservation equation, and time-dependent evolution equation of magnetic field are used to describe the evolution of the benchmark SNR with time:

$$\frac{\partial \rho}{\partial t} + \nabla \cdot (\rho \boldsymbol{v}) = 0 \tag{4}$$

$$\frac{\partial \rho \boldsymbol{v}}{\partial t} + \nabla \cdot (\rho \boldsymbol{v}\boldsymbol{v} - \boldsymbol{B}\boldsymbol{B}) + \nabla P^* = 0, \tag{5}$$

$$\frac{\partial E}{\partial t} + \nabla \cdot [(E + P^*)\boldsymbol{v} - \boldsymbol{B}(\boldsymbol{v} \cdot \boldsymbol{B})] = 0, \tag{6}$$

$$\frac{\partial \boldsymbol{B}}{\partial t} + \nabla \times (\boldsymbol{v} \times \boldsymbol{B}) = 0, \tag{7}$$

where ρ, $\boldsymbol{v}$, $\boldsymbol{B}$, and $P^* = P + B^2/8\pi$ are the mass density, gas velocity, magnetic field, and total pressure (thermal pressure P adds the magnetic pressure $B^2/8\pi$), respectively. The total energy density E is expressed as:

$$E = \frac{P}{\gamma_{\rm eff} - 1} + \frac{1}{2}\rho v^2 + \frac{B^2}{8\pi}, \tag{8}$$

where $\gamma_{\rm eff}$ is the effective adiabatic index. We consider four different $\gamma_{\rm eff}$ here, namely $\gamma_{\rm eff} = 5/3$, 4/3, 1.2, and 1.1.

The PLUTO code developed by Mignone et al. (2007, 2012), with the cell-centered finite-volume scheme as the main method to solve MHD equations, is adopted to perform our simulations: (i) the simulations are carried out in the cylindrical coordinate system with 1024×2048 uniform cells; (ii) the Eight-Wave Formulation is used to keep $\nabla \cdot \boldsymbol{B} = 0$, while HLLC Riemann solver is set to calculate the flux. We assign reflective boundary conditions at $R = 0$ (the z-axis), and outflow conditions for other boundaries, respectively. In this paper, the end time of simulations is set as 1 kyr and we do not consider the radiative cooling as the benchmark SNR is still in its adiabatic stage (Blondin et al. 1998; Petruk 2005).

2.3. Initial Background Magnetic Field

In this paper, we introduce two different BMF topologies (Schure et al. 2009):

(1) The B_z case: a uniform BMF of $B_0 = 3\ \mu$G parallel to the z-direction (Beck 2016; Han 2017).

(2) The $B_{\rm tur}$ case: a Kolmogorov-like turbulent magnetic field, i.e., a uniform large-scale field $B_0 = 3\ \mu$G with a component $\delta\boldsymbol{B}(r, z)$ described as:

$$\begin{aligned} \delta\boldsymbol{B}(r, z) = &\sum_{n=1}^{N_m} \sqrt{C_{\rm B} 2\pi k_n \Delta k_n P_{\rm B}(k_n)} \\ &\times (\sin\theta_n \hat{r} - \cos\theta_n \hat{z}) \times \exp[i(\cos\theta_n k_n r \\ &+ \sin\theta_n k_n z + \phi_n)], \end{aligned} \tag{9}$$

where $C_{\rm B}$ is the normalization constant; θ_n is the random propagation angle and ϕ_n is the random phase. $P_{\rm B}$ is the power function for wave mode with a wavenumber of k_n:

$$P_{\rm B}(k_n) \propto \frac{1}{1 + (k_n L)^{\Gamma}}; \tag{10}$$

where the coherence length L is 3 pc and the spectral index Γ is 8/3 (see Guo et al. 2012 and Wang et al. 2018 for more details). Thereby, $C_{\rm B}$ here is $0.5823 \times 10^{-12}\ {\rm pc}^2\ {\rm G}^2$ (G stands for Gauss).

Figure 1 describes the two initial BMFs that we calculated in advance, where the white arrows represent the local magnetic-field lines. The data is expressed logarithmically in units of μG to highlight the turbulent magnetic field.

[3] The units of ρ_c and $\rho_{\rm ej}$ are g ${\rm s}^3$ ${\rm cm}^{-3}$ and g ${\rm cm}^{-3}$, respectively.
[4] Thus, v_c and $v_c t$ are 7.7×10^8 cm ${\rm s}^{-1}$ and 2.2×10^{17} cm, respectively.

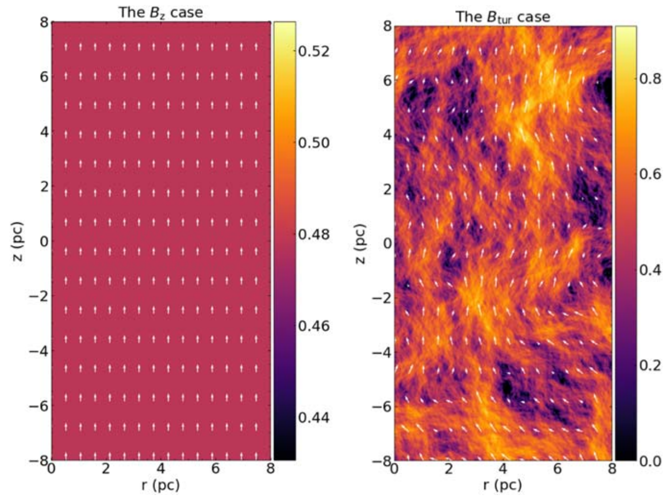

Figure 1. Schematic diagrams of background magnetic fields in two cases. The left and right panels are for the B_z and $B_{\rm tur}$ cases, respectively. The white arrows represent the local magnetic-field lines. The color bars show the logarithm of the magnetic fields in units of μG.

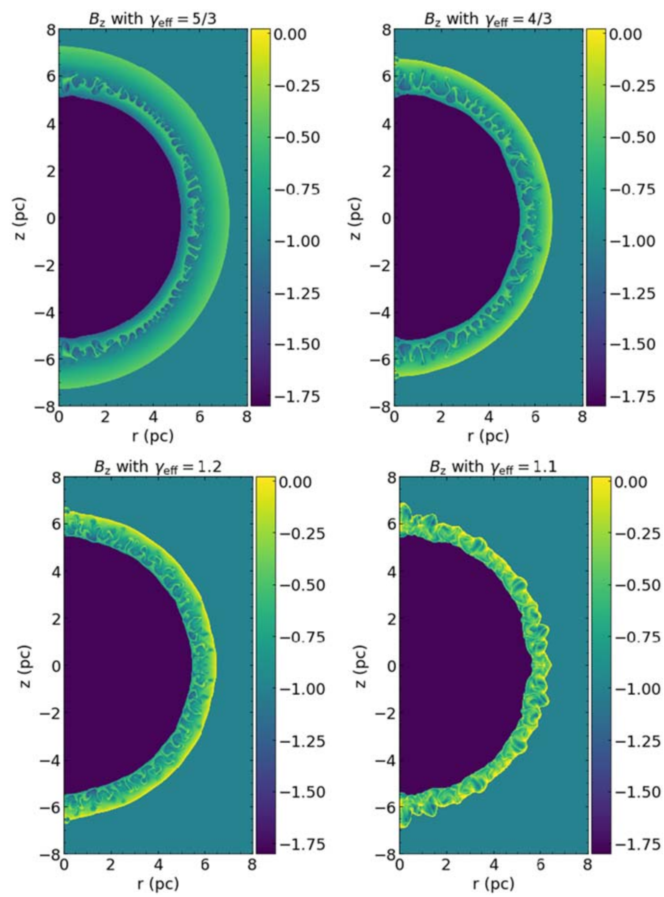

Figure 2. Density profiles of the benchmark SNR at 1 kyr with $\gamma_{\rm eff} = 5/3$, $4/3$, 1.2, and 1.1 for the B_z case. The color bars show the logarithm of density in units of $m_{\rm H}$ cm^{-3}.

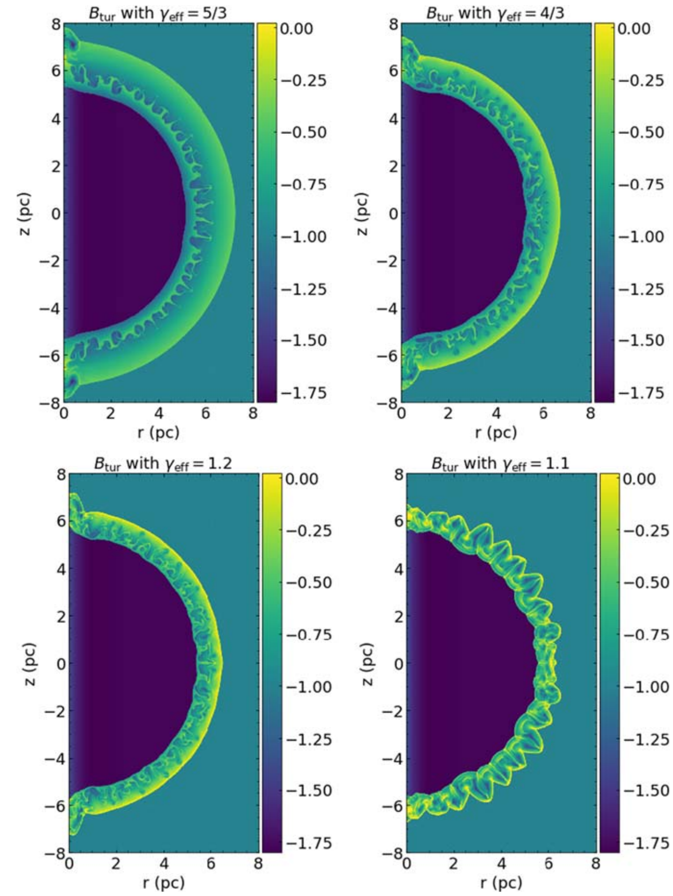

Figure 3. Density profiles of the benchmark SNR at 1 kyr with $\gamma_{\rm eff} = 5/3$, $4/3$, 1.2, and 1.1 for the $B_{\rm tur}$ case. The color bars show the logarithm of density in units of $m_{\rm H}$ cm^{-3}.

3. Results

3.1. Density Profiles

Figures 2 and 3 portray the density distribution of the benchmark SNR under two different BMFs at $t = 1$ kyr. In order to show the structure of the SNR more clearly, the logarithm is taken. In both cases, the two-shock structure is evident. As $\gamma_{\rm eff}$ decreases from $5/3$ to 1.2, the FS radius decreases while the RS radius increases (see also Figure 4),[5] leading to the shrinking of the two-shock structure gradually. For $\gamma_{\rm eff} = 1.2$, some RT fingers reach the FS and cause some slight protrusions, appearing as the fluctuations in the azimuthal variations of the FS radius in Figure 4. While with $\gamma_{\rm eff} = 1.1$, RT fingers push small regions out ahead of the average shock radius, distorting the FS and engendering a mixture between the shocked ISM and the ejecta.

[5] We note that, in the density profiles of the benchmark SNR, some jet-like structures near the z-direction give rise to mushroom-shaped clouds in the north of the SNR. These structures which are within an angular interval of $\sim 10°$ with regard to the z-direction are numerical artifacts and not real (Dwarkadas 2000). Hence, in this paper, we only extract and analyze the physical information of our benchmark SNR in the angular interval between $\pm 80°$ from the r-direction.

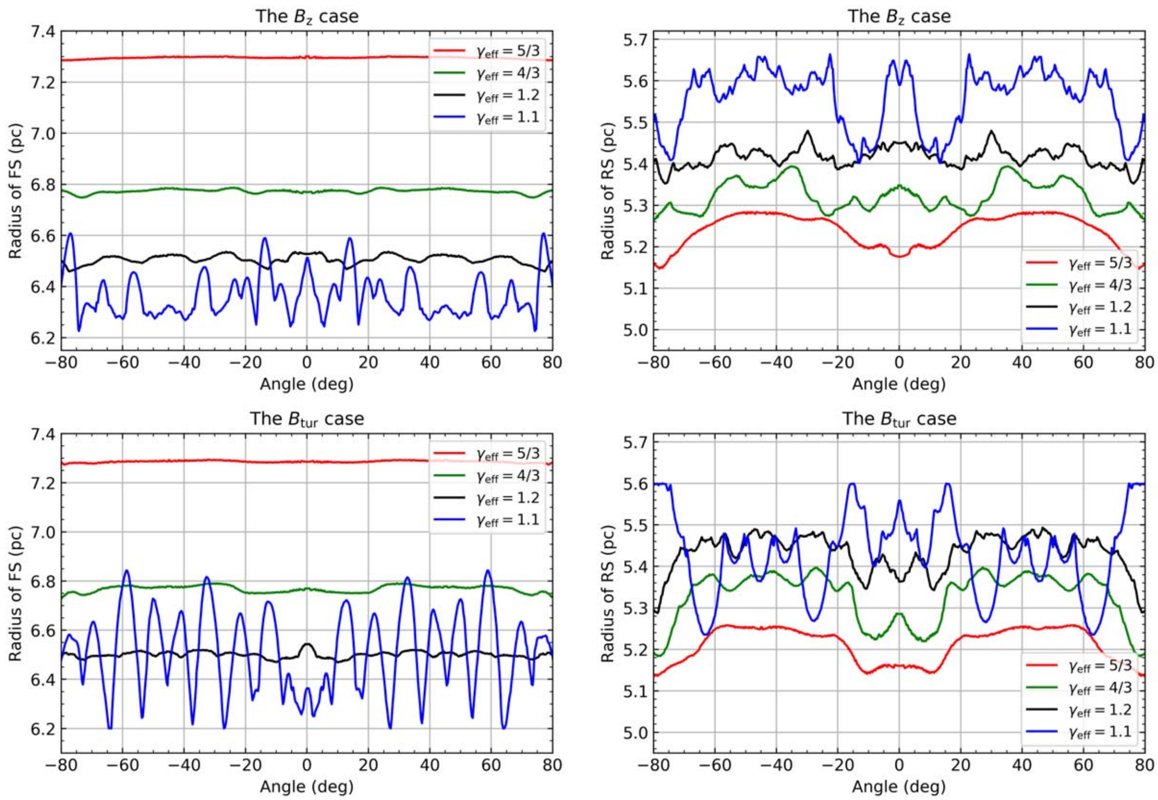

Figure 4. The location of the forward shock and reverse shock at different angles with regard to the r-direction (in a counterclockwise direction). The top and bottom panels are for the B_z case and the B_{tur} case, respectively.

As a result, the two-shock structure is deformed and the overall outline displays significant deviations from sphericity. These results are consistent with the findings in Blondin & Ellison (2001), Orlando et al. (2012), and Warren & Blondin (2013). Regarding the density profiles and two-shock structures, the morphologies of benchmark SNR in different BMF cases are qualitatively similar.

3.2. Magnetic-field Structure

Figures 5 and 6 display the spatial magnetic-field structure of our benchmark SNR with different BMFs at $t = 1$ kyr. For both cases, the magnetic fields in the two-shock structure are notably higher than those in other areas, due to the shock compression and the amplification effects of RTI. The intershock region gets brighter when $\gamma_{\rm eff}$ decreases, because of the increased shock compression ratio. Besides, owing to the fast outward expansion, the magnetic fields are weak inside the unshocked ejecta.

For the B_z case (panels in Figure 5), since the BMF is homogeneous along the z-direction, the projected value of the BMF in the tangential direction of FS drops from the equator to the poles, resulting in a brighter region at the equator. This is also distinctly shown by the lengths of the white arrows, which characterize the local magnetic-field lines in the shocked region. We notice that most arrows in the immediate FS downstream exhibit tangential orientations when $\gamma_{\rm eff}$ is $5/3$. However, the arrow orientations are disordered within the RT structures, and some of them are virtually radial. The number of tangential arrows in the downstream decreases as the volume of the shocked ISM reduces at $\gamma_{\rm eff} = 4/3$. Meanwhile, there appears to be a greater diversity in the orientations of the arrows in the RT structures, with more nearly radial arrows showing up. For $\gamma_{\rm eff} = 1.2$ and 1.1, a further shrunk intershock region leads to fewer tangential arrows. Accordingly, the magnetic-field orientation in the intershock region depends on the relative contributions from the RTI and shocked ISM. When $\gamma_{\rm eff}$ decreases, the magnetic-field orientation is principally dominated by the RTI.

Concerning the $B_{\rm tur}$ case, as depicted in the panels in Figure 6, the prespecified large-scale magnetic-field fluctuations are apparent. On account of the turbulent components in the BMF, some irregular dark regions exist in the intershock region, while some RTI regions are brighter compared with those in the B_z case. However, for each $\gamma_{\rm eff}$, the overall distribution of the magnetic-field orientation in the intershock region is similar with its counterpart in the B_z case.

To acquire more information about the magnetic-field structure in the intershock region, we intend to analyze the

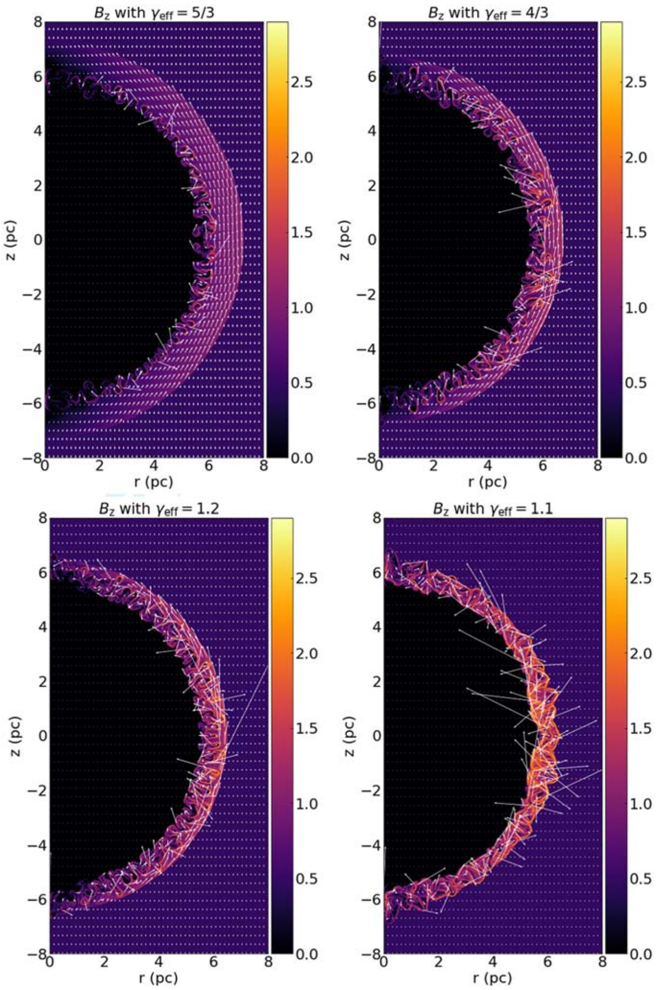

Figure 5. Magnetic-field structure of our benchmark SNR at 1 kyr for $\gamma_{\rm eff} = 5/3$, $4/3$, 1.2, and 1.1 in the B_z case. The color bars show the logarithm of magnetic fields in units of μG. The white arrows represent the local magnetic-field lines.

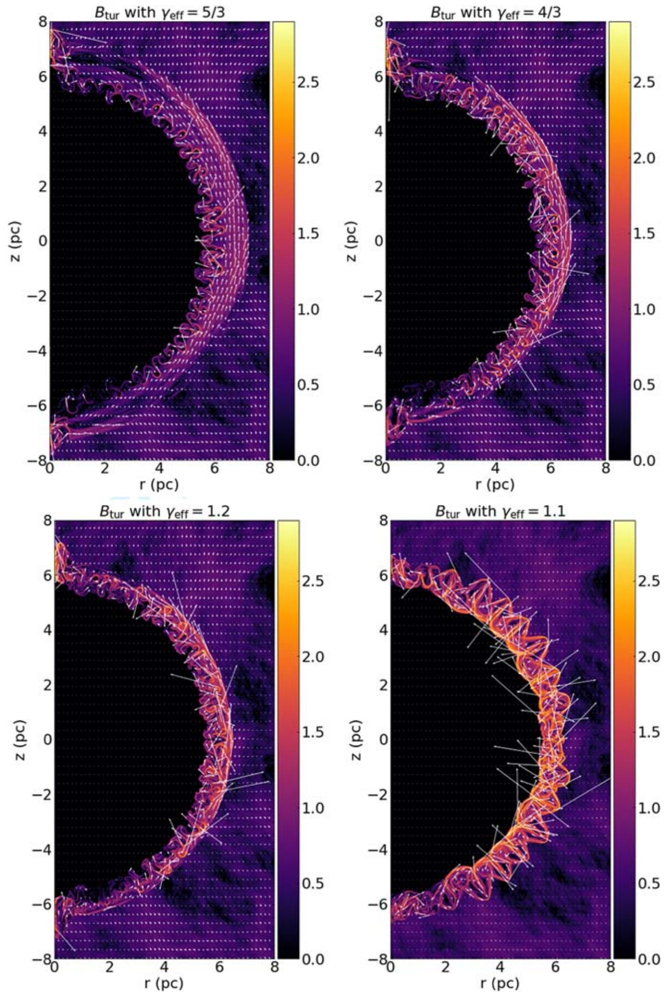

Figure 6. Magnetic-field structure of our benchmark SNR at 1 kyr for $\gamma_{\rm eff} = 5/3$, $4/3$, 1.2, and 1.1 in the $B_{\rm tur}$ case. The color bars show the logarithm of magnetic fields in units of μG. The white arrows represent the local magnetic-field lines.

magnetic-field orientation as a function of time. We denote the total number of grid cells located in the intershock region as $n_{\rm total}$.[6] Among these cells, those whose magnetic-field orientation makes an angle less than 45° with the local radial direction are defined as the "cells with quasi-radial magnetic fields," with their quantity marked as n_{45}. We use the ratio of n_{45} to $n_{\rm total}$ to describe the proportion of the cells with quasi-radial magnetic fields to the total cells during the SNR evolution. This ratio versus time is displayed in Figure 7 for four values of $\gamma_{\rm eff}$ for the B_z and $B_{\rm tur}$ cases, respectively.

As shown in the left panel of Figure 7 (the B_z case), it is evident that, as $\gamma_{\rm eff}$ reduces, the regions with quasi-radial magnetic fields take up a larger proportion of the intershock region after $t = 200$ yr.[7] This is mainly due to the growth of RTI and the magnetic-field structure in situ. More explicitly, on one hand, the RTI could be enhanced if a lower $\gamma_{\rm eff}$ is considered (Decourchelle et al. 2000; Fraschetti et al. 2010; Peng et al. 2020). As a consequence, the developed finger-like structures will further stretch local magnetic field lines preferentially along the radial direction (Gull & Longair 1973; Jun & Norman 1996b; Dubner & Giacani 2015). On the other hand, with a decreasing $\gamma_{\rm eff}$, the volume of the shocked ISM is reduced, where the tangential magnetic field prevails. In the right panel of Figure 7, the overall tendency of the lines with various

[6] In preparation for a more comprehensive explanation of our results, the definitions and expressions of physical quantities utilized in this article are presented in the Appendix. We detect the positions of FS and RS based on the pressure jump caused by the shocks, and the region between the FS and RS is the intershock region.

[7] We start our analysis at $t = 200$ yr when the RT finger-like structures for the two cases are well developed, as we tend to study the influences on the magnetic field orientation exerted by those subtle structures.

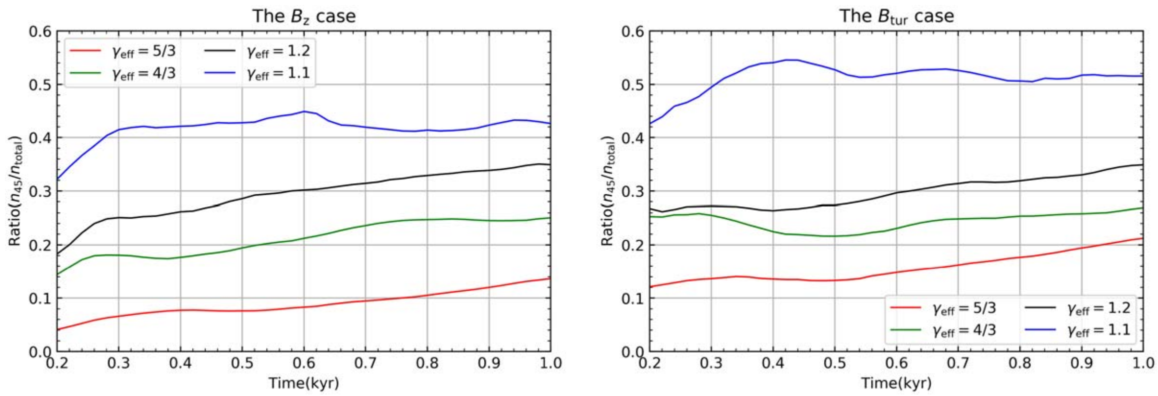

Figure 7. The ratio n_{45}/n_{total} vs. time for the B_z (left panel) and B_{tur} (right panel) cases.

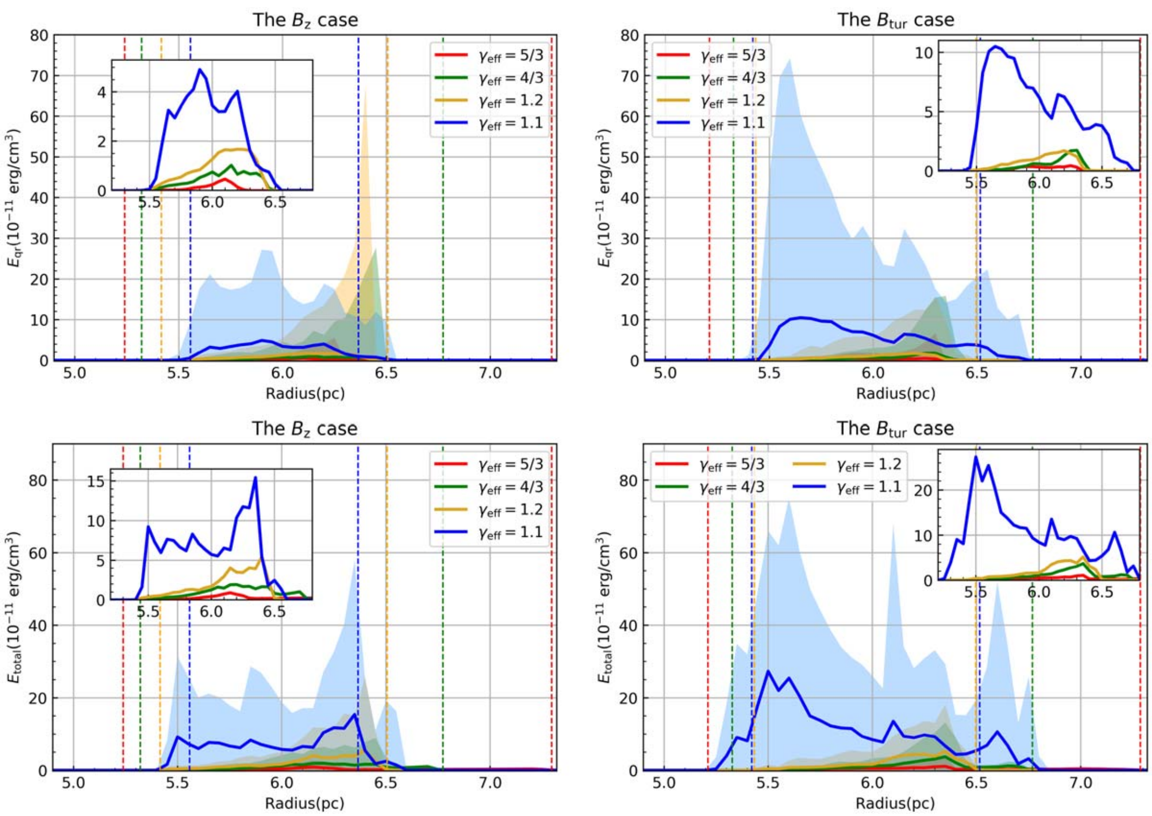

Figure 8. Top panels: the quasi-radial magnetic energy density E_{qr} in each radial interval vs. the radius in the B_z (top left panel) and B_{tur} (top right panel) cases. Bottom panels: the total magnetic energy density E_{total} in each radial interval vs. the radius in the B_z (bottom left panel) and B_{tur} (bottom right panel) cases. The shaded areas, with identical colors as the curves, correspond to the standard deviation of E_{qr} and E_{total}. The dashed lines, sharing the same colors with the curves, are the averaged positions of FS and RS with different γ_{eff}, respectively.

γ_{eff} for the B_{tur} case is similar to that of the B_z case. Thereby, under the efficient shock acceleration, there appear to be more quasi-radial magnetic fields within the SNR in the two cases.

Figures 8 and 9 are plotted to assess the feedback of efficient shock acceleration on the magnetic energy density within the two-shock structure. Specifically, Figure 8 shows the quasi-radial magnetic energy density E_{qr} (top two panels) and the total magnetic energy density E_{total} (bottom two panels) in each radial interval (between R and R+0.05 pc). The shaded areas, with identical colors as the curves, correspond to the standard deviation of E_{qr} and E_{total}, respectively. In a given radial interval, a large standard deviation suggests a high dispersion of the magnetic energy densities, while a small standard deviation means a low dispersion. More explicitly, in the unstable region, there exists a substantial disparity in magnetic field strengths among different grid cells, leading to a

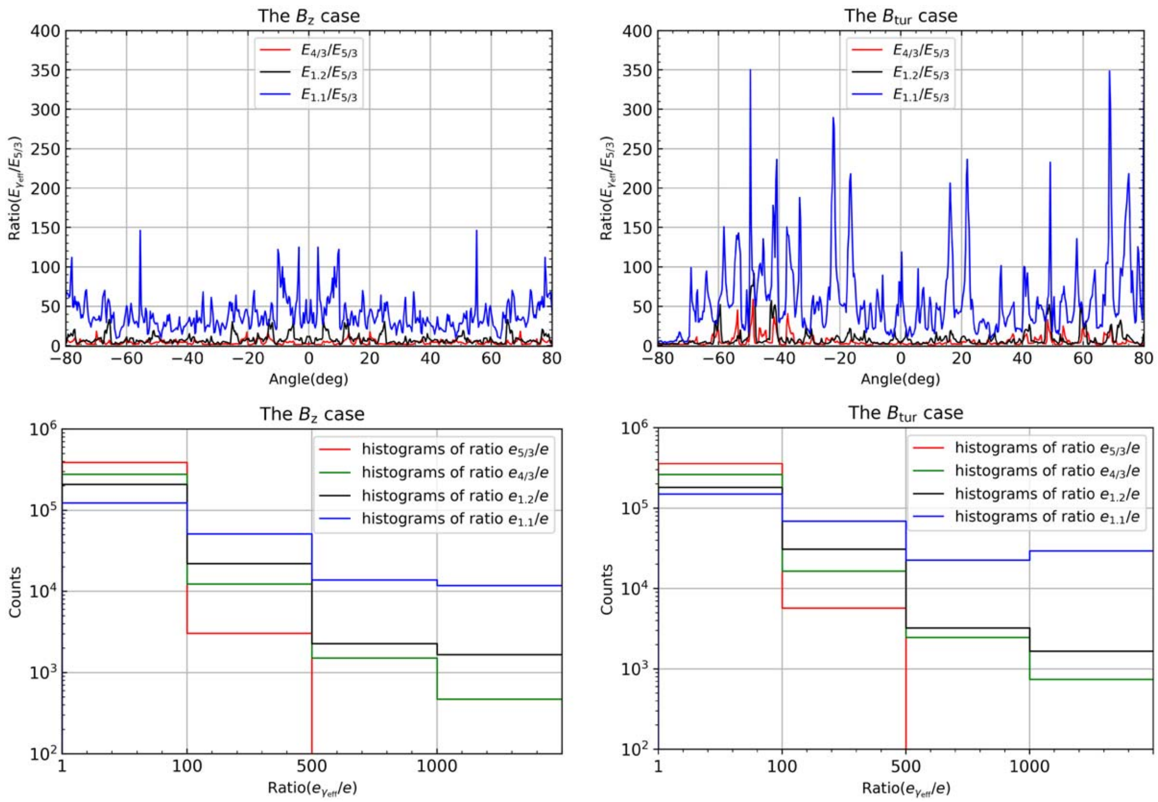

Figure 9. Top panels: the azimuthal distributions of ratio $E_{\gamma_{\rm eff}}/E_{5/3}$ for the B_z (top left panel) and $B_{\rm tur}$ (top right panel) cases, where $E_{\gamma_{\rm eff}}$ is the total magnetic energy density in each angular interval (0°.6) with $\gamma_{\rm eff}$. Bottom panels: the histograms of the ratio $e_{\gamma_{\rm eff}}/e$ in the B_z (bottom left panel) and $B_{\rm tur}$ (bottom right panel) cases, where $e_{\gamma_{\rm eff}}$ is the magnetic energy density of each grid cell in the shocked region with $\gamma_{\rm eff}$ and e is the background magnetic energy density ($B_0 = 3\ \mu$G).

large standard deviation in magnetic field densities. Whereas, the magnetic field strengths of the cells in the unshocked regions demonstrate a slight disparity in magnetic field strengths, so the standard deviation of the magnetic field densities there is small. As $\gamma_{\rm eff}$ decreases, peak values of both $E_{\rm qr}$ and $E_{\rm total}$ rise, implying stronger quasi-radial magnetic energy density and total magnetic energy density. With regard to the uniform case, the peak value of $E_{\rm qr}$ with $\gamma_{\rm eff} = 1.1$ (4.9×10^{-11} erg cm^{-3}) is $\sim$10 times that with $\gamma_{\rm eff} = 5/3$ (0.5×10^{-11} erg cm^{-3}). While for the turbulent case, the peak value of $E_{\rm qr}$ with $\gamma_{\rm eff} = 1.1$ (10.5×10^{-11} erg cm^{-3}) is $\sim$26.3 times that with $\gamma_{\rm eff} = 5/3$ (0.4×10^{-11} erg cm^{-3}). As for $E_{\rm total}$, the apex value of $E_{\rm total}$ is 15.4×10^{-11} erg cm^{-3} in the uniform case with $\gamma_{\rm eff} = 1.1$, $\sim$17.1 times that in the same case with $\gamma_{\rm eff} = 5/3$ (0.9×10^{-11} erg cm^{-3}). Concerning the turbulent case, the apex value of $E_{\rm total}$ is 27.3×10^{-11} erg cm^{-3} with $\gamma_{\rm eff} = 1.1$, $\sim$24.8 times that with $\gamma_{\rm eff} = 5/3$ (1.1×10^{-11} erg cm^{-3}).

In the shocked region, we denote the total magnetic energy density in each angular interval (0°.6) with $\gamma_{\rm eff}$ as $E_{\gamma_{\rm eff}}$. The ratio of $E_{\gamma_{\rm eff}}$ to $E_{5/3}$ is adopted in each angular interval to quantify the MFA owing to the efficient shock acceleration. The top two images in Figure 9. depict the azimuthal distributions of ratios $E_{4/3}/E_{5/3}$, $E_{1.2}/E_{5/3}$, and $E_{1.1}/E_{5/3}$ for both cases. We find that values of ratio $E_{1.1}/E_{5/3}$ within angular intervals are generally higher than those of ratios $E_{4/3}/E_{5/3}$ and $E_{1.2}/E_{5/3}$ for both cases, revealing more efficient field amplification. The maximum value of ratio $E_{1.1}/E_{5/3}$ achieved in the simulations is about 350. In the bottom panels of Figure 9, the histograms of the ratio $e_{\gamma_{\rm eff}}/e$ are illustrated, serving as an indicator for MFA in the intershock region. Here, $e_{\gamma_{\rm eff}}$ symbolizes the magnetic energy density of each grid cell in the shocked region with $\gamma_{\rm eff}$, while e is the background magnetic energy density ($B_0 = 3\ \mu$G). As shown in the plots, the magnetic energy densities of quite a few cells are amplified over 1000 times in both cases. With a declining $\gamma_{\rm eff}$, there exist reductions in the counts of lower ratios ($<$100), along with increases in the counts of ratios exceeding 100 times. Our quantitative results suggest that, for both uniform and turbulent BMFs, when the shock acceleration is efficient, the magnetic energy density inside the intershock region is enhanced.

Summarizing our results, a lower $\gamma_{\rm eff}$ contributes to the changes in the downstream magnetic-field structure for both B_z and $B_{\rm tur}$ cases, inducing the enhancements of magnetic energy density within the intershock region.

4. Conclusions and Discussion

The shock acceleration process could affect the two-shock structure as well as the magnetic fields inside type Ia SNRs, demonstrated by recent numerical simulations (Orlando et al. 2012; Warren & Blondin 2013; Peng et al. 2020). Besides, foregoing research implies that the magnetic-field structure in cosmic space is complex (Parker 1958; Beck 2016; Han 2017; Shimoda et al. 2018; Saha et al. 2019), indicating different BMF topologies. Based on a series of 2D MHD simulations in a cylindrical coordinate system, investigations on the downstream magnetic-field structure of young type Ia SNRs with two different BMFs have been made. In this work, a uniform and a turbulent BMF are considered, and an effective adiabatic index $\gamma_{\rm eff}$ is adopted to mimic the feedback of the shock acceleration.

Initially, we present the density profiles and the magnetic-field structure of the benchmark SNR at $t = 1$ kyr for both cases with different $\gamma_{\rm eff}$. In Figures 2 and 3, the two-shock structure is obtained, which shrinks with a decreasing $\gamma_{\rm eff}$ (from $5/3$ to 1.2). While with $\gamma_{\rm eff} = 1.1$, the two-shock structure is severely deformed and the overall outline displays significant deviations from sphericity (see also Figure 4). Regarding the two different BMFs considered here, their resulting density profiles in the intershock region are qualitatively similar. Figures 5 and 6 illustrate the magnetic-field structure for our benchmark SNR. If a lower $\gamma_{\rm eff}$ is taken, the magnetic fields in the immediate shock downstream are further compressed, and the overall magnetic-field orientation appears to be further disordered.

Furthermore, Figures 7–9 analyze the orientation distribution and the energy density of the downstream magnetic fields in our benchmark SNR. We employ the ratio $n_{45}/n_{\rm total}$ to characterize the magnetic-field orientation distribution in the shocked region. Within the intershock region, the total number of grid cells is denoted as $n_{\rm total}$, while n_{45} is defined as the "quasi-radial magnetic field" cell number. Our results reveal that the feedback of efficient shock acceleration ($\gamma_{\rm eff} < 5/3$) is capable to modify the downstream magnetic-field structure of our benchmark SNR (Figure 7), resulting in more quasi-radial magnetic fields inside the intershock region. To describe the magnetic energy density inside the intershock region, we plot $E_{\rm qr}$ and $E_{\rm total}$ versus radius (Figure 8) as well as the azimuthal distributions of ratio $E_{\gamma_{\rm eff}}/E_{5/3}$ and the histograms of ratio $e_{\gamma_{\rm eff}}/e$ (Figure 9). For both uniform and turbulent BMFs, peak values of $E_{\rm qr}$ with $\gamma_{\rm eff} = 1.1$ are 10–26 times those with $\gamma_{\rm eff} = 5/3$, while the apex values of $E_{\rm total}$ with $\gamma_{\rm eff} = 1.1$ are 17–25 times those with $\gamma_{\rm eff} = 5/3$. Concerning $E_{\gamma_{\rm eff}}$ and $e_{\gamma_{\rm eff}}$, it is noteworthy that with a lower $\gamma_{\rm eff}$, $E_{\gamma_{\rm eff}}$ could be amplified by more than 350 times, while $e_{\gamma_{\rm eff}}$ of more cells could be magnified over 1000 times. Our results suggest that the efficient shock-acceleration feedback would increase the magnetic energy density within the shocked region. Additionally, it is worth noting that the resolution employed in simulation runs could influence the MFA. With higher grid resolution, the magnetic-field strength in the intershock region would increase, attributed to the enhancement of turbulent amplification of magnetic field and the reduction of numerical dissipation (Jun & Norman 1996b; Guo et al. 2012).

According to the theory of DSA, the particles are thought to be accelerated through efficient scattering by magnetic turbulence near the shock front (Reynolds 2008; Morlino 2017). Due to multiple scattering, particles repeatedly diffuse across the shock front and collide with scattering centers in both the upstream and downstream flows (Amato 2014; Xu & Lazarian 2022). In the shock downstream, the magnetic turbulence is mainly triggered by hydrodynamical instabilities, owing to distortions of magnetic-field lines by vortices in the RT unstable region (Gull & Longair 1973; Jun et al. 1996; Giacalone & Jokipii 2007; Inoue et al. 2009). Since the efficient shock acceleration leads to RT fingers approaching the shock front, more magnetic turbulence is expected to appear in the immediate shock downstream. This may promote the scattering efficiency in the downstream and increase the probability of particles to recross the shock front. Therefore, for young type Ia SNRs, the quasi-radial magnetic field (both orientation and energy) and relative positions of the CD (ratio of the forward shock radius to the contact discontinuity) (Bao et al. 2021), could serve as observational diagnostics of efficient shock acceleration.

As previous MHD simulations proclaim, during the temporal evolution of an SNR, the RTI could vary the magnetic-field structure in the shocked region, and there are copious factors that may induce the development of RTI. Pressure gradients, circumstellar cloudlets, and the high-density ejecta clumps approaching the CD will contribute to faster growth rates and larger amplitudes for RT fingers (Jun et al. 1996; Decourchelle et al. 2000; Orlando et al. 2012), leading to modifications in the magnetic-field structure inside an SNR. Besides, lowering $\gamma_{\rm eff}$, which signifies that the impacts from particle escape and relativistic particle pressure take place everywhere, is only an approximation for mimicking the feedback of effective shock acceleration (Blondin & Ellison 2001; Wang 2011). It engenders an elevation in the shock compression ratio, thereby changing the morphology and magnetic-field structure of our benchmark SNR. The MFA occurring in the shocked region is owing to the heightened compression ratio and enhanced RTI. Given that the shock-acceleration process depends on specific physical parameters (such as shock velocity and the injection rate of particles), more realistic processes that may impact the magnetic-field structure of SNRs deserve a further detailed study, which could provide a deeper understanding toward the evolution of young type Ia SNRs.

Acknowledgments

This work is partially supported by the National Natural Science Foundation of China 12233006. B.W.B. is partially supported by the National Natural Science Foundation of China 12203042, and the Foundations of Yunnan Province 202301AU070009.

Appendix
Definitions and Expressions of the Utilized Physical Quantities

Table A1 includes the physical quantities that we utilized in this article, as well as their definitions and expressions.

Table A1
Physical Quantities and their Definitions

Physical Quantities	Definitions	Expressions
r	the abscissa in a cylindrical coordinate system.	⋯
z	the ordinate in a cylindrical coordinate system.	⋯
R	radius from the coordinate origin (0,0).	$R = \sqrt{r^2 + z^2}$
θ	angle from the r-direction (in a counterclockwise direction).	⋯
B_i	magnetic field strength of each grid cell.	⋯
B_n	quasi-radial magnetic field strength. If the magnetic-field orientation of a given grid cell makes an angle less than 45° with the local radial direction, the magnetic field in that situation is defined as the "quasi-radial magnetic field."	⋯
$n_{\rm total}$	number of cells whose center is located within the shocked region.	
n_{45}	number of cells with quasi-radial magnetic fields among $n_{\rm total}$.	⋯
ΔV_i	volume of a given grid cell in the cylindrical coordinate system.	$\Delta V_i = 2\pi r_i dr_i dz_i$
ΔV_n	volume of a given grid cell with a quasi-radial magnetic field.	$\Delta V_n = 2\pi r_n dr_n dz_n$
$E_{\rm total}$	total magnetic energy density in each radial interval ($\Delta R = 0.05$ pc).	$E_{\rm total} = \frac{\sum_i \frac{B_i^2}{8\pi}\Delta V_i}{\sum_i \Delta V_i}$
$E_{\rm qr}$	quasi-radial magnetic energy density in each radial interval ($\Delta R = 0.05$ pc).	$E_{\rm qr} = \frac{\sum_n \frac{B_n^2}{8\pi}\Delta V_n}{\sum_i \Delta V_i}$
$E_{\rm eff}$	total magnetic energy density in each angular interval ($\Delta\theta = 0\overset{\circ}{.}6$) inside the shocked region with $\gamma_{\rm eff}$.	$E_{\rm eff} = \frac{\sum_i \frac{B_i^2}{8\pi}\Delta V_i}{\sum_i \Delta V_i}$
$e_{\rm eff}$	magnetic energy density of each grid cell inside the shocked region with $\gamma_{\rm eff}$.	$e_{\rm eff} = \frac{B_i^2}{8\pi}$
e	the background magnetic energy density ($B_0 = 3\ \mu$G).	$\frac{B_0^2}{8\pi}$

References

Acciari, V. A., Aliu, E., Arlen, T., et al. 2011, ApJL, 730, L20
Acero, F., Aharonian, F., Akhperjanian, A. G., et al. 2010, A&A, 516, A62
Amato, E. 2014, IJMPD, 23, 1430013
Baade, W., & Zwicky, F. 1934, PNAS, 20, 259
Balsara, D., Benjamin, R. A., & Cox, D. P. 2001, ApJ, 563, 800
Bao, B. W., Peng, Q. Y., Yang, C. Y., & Zhang, L. 2021, ApJ, 909, 173
Bao, B. W., Yang, C. Y., & Zhang, L. 2018, ApJ, 866, 37
Beck, R. 2016, A&ARv, 24, 4
Bell, A. R. 1978, MNRAS, 182, 147
Bell, A. R. 2004, MNRAS, 353, 550
Bell, A. R. 2013, APh, 43, 56
Blasi, P. 2013, A&ARv, 21, 70
Blondin, J. M., & Ellison, D. C. 2001, ApJ, 560, 244
Blondin, J. M., Wright, E. B., Borkowski, K. J., & Reynolds, S. P. 1998, ApJ, 500, 342
Cardillo, M., Tavani, M., Giuliani, A., et al. 2014, A&A, 565, A74
Chevalier, R. A. 1982, ApJ, 258, 790
Chevalier, R. A. 1983, ApJ, 272, 765
Decourchelle, A., Ellison, D. C., & Ballet, J. 2000, ApJL, 543, L57
DeLaney, T., Koralesky, B., Rudnick, L., & Dickel, J. R. 2002, ApJ, 580, 914
Dickel, J. R., & Milne, D. K. 1976, AuJPh, 29, 435
Dubner, G., & Giacani, E. 2015, A&ARv, 23, 3
Dwarkadas, V. V. 2000, ApJ, 541, 418
Dwarkadas, V. V., & Chevalier, R. A. 1998, ApJ, 497, 807
Ferrand, G., Decourchelle, A., Ballet, J., et al. 2010, A&A, 509, L10
Fraschetti, F., Teyssier, R., Ballet, J., & Decourchelle, A. 2010, A&A, 515, A104
Giacalone, J., & Jokipii, J. R. 2007, ApJL, 663, L41
Gull, S. F., & Longair, M. S. 1973, MNRAS, 161, 47
Guo, F., Li, S., Li, H., et al. 2012, ApJ, 747, 98
Han, J. L. 2017, ARA&A, 55, 111
Hu, Y., Xu, S., Stone, J. M., & Lazarian, A. 2022, ApJ, 941, 133
Inoue, T., Shimoda, J., Ohira, Y., & Yamazaki, R. 2013, ApJL, 772, L20
Inoue, T., Yamazaki, R., & Inutsuka, S. 2009, ApJ, 695, 825
Jun, B.-I., & Jones, T. W. 1999, ApJ, 511, 774
Jun, B.-I., Jones, T. W., & Norman, M. L. 1996, ApJL, 468, L59
Jun, B.-I., & Norman, M. L. 1996a, ApJ, 465, 800
Jun, B.-I., & Norman, M. L. 1996b, ApJ, 472, 245
Jun, F., & Li, Z. 2012, MNRAS, 424, 2811
Lopez, L. A., Ramirez-Ruiz, E., Huppenkothen, D., et al. 2011, ApJ, 732, 114
Lucek, S. G., & Bell, A. R. 2000, MNRAS, 314, 65
McKee, C. F. 1974, ApJ, 188, 335
McKee, C. F., & Truelove, J. K. 1995, PhR, 256, 157
Mignone, A., Bodo, G., Massaglia, S., et al. 2007, ApJS, 170, 228
Mignone, A., Zanni, C., Tzeferacos, P., et al. 2012, ApJS, 198, 7
Morlino, G. 2017, in IAU Symp. 331, Supernova 1987A: 30 years Later—Cosmic Rays and Nuclei from Supernovae and their Aftermaths, ed. A. Marcowith et al. (Cambridge: Cambridge Univ. Press), 230
Orlando, S., Bocchino, F., Miceli, M., Petruk, O., & Pumo, M. L. 2012, ApJ, 749, 156
Orlando, S., Bocchino, F., Reale, F., Peres, G., & Petruk, O. 2007, A&A, 470, 927

Orlando, S., Miceli, M., Petruk, O., et al. 2019, A&A, 622, A73
Orlando, S., Petruk, O., Bocchino, F., & Miceli, M. 2011, A&A, 526, A129
Parker, E. N. 1958, ApJ, 128, 664
Peng, Q. Y., Bao, B. W., Yang, C. Y., & Zhang, L. 2020, ApJ, 891, 75
Petruk, O. 2005, JPhSt, 9, 364
Petruk, O., Kuzyo, T., & Beshley, V. 2016, MNRAS, 456, 2343
Petruk, O., Kuzyo, T., Orlando, S., Pohl, M., & Brose, R. 2021, MNRAS, 505, 755
Petruk, O., Kuzyo, T., Orlando, S., et al. 2018, MNRAS, 479, 4253
Reynolds, S. P. 2008, ARA&A, 46, 89
Reynolds, S. P. 2017, in Handbook of Supernovae, ed. A. W. Alsabti & P. Murdin (Berlin: Springer), 1981
Reynoso, E. M., Hughes, J. P., & Moffett, D. A. 2013, AJ, 145, 104
Reynoso, E. M., Moffett, D. A., Goss, W. M., et al. 1997, ApJ, 491, 816
Riquelme, M. A., & Spitkovsky, A. 2009, ApJ, 694, 626
Saha, P., Bharadwaj, S., Roy, N., et al. 2019, MNRAS, 489, 5866
Schure, K. M., Bell, A. R., O'C Drury, L., et al. 2012, SSRv, 173, 491
Schure, K. M., Vink, J., Achterberg, A., & Keppens, R. 2009, AdSpR, 44, 433
Shimoda, J., Akahori, T., Lazarian, A., Inoue, T., & Fujita, Y. 2018, MNRAS, 480, 2200
Shin, M.-S., Stone, J. M., & Snyder, G. F. 2008, ApJ, 680, 336
Telezhinsky, I., Dwarkadas, V. V., & Pohl, M. 2013, A&A, 552, A102
Vink, J. 2020, in Physics and Evolution of Supernova Remnants, ed. M. A. Barstow, A. Burkert, A. Coustenis et al. (Berlin: Springer), 56
Vink, J., & Laming, J. M. 2003, ApJ, 584, 758
Völk, H. J., Berezhko, E. G., & Ksenofontov, L. T. 2005, A&A, 433, 229
Wang, C.-Y. 2011, MNRAS, 415, 83
Wang, C.-Y., & Chevalier, R. A. 2001, ApJ, 549, 1119
Wang, Y. Y., Bao, B. W., Yang, C. Y., & Zhang, L. 2018, MNRAS, 478, 2948
Warren, D. C., & Blondin, J. M. 2013, MNRAS, 429, 3099
Warren, J. S., Hughes, J. P., Badenes, C., et al. 2005, ApJ, 634, 376
West, J. L., Safi-Harb, S., & Ferrand, G. 2016, A&A, 597, A121
Xu, S., & Lazarian, A. 2016, ApJ, 833, 215
Xu, S., & Lazarian, A. 2022, ApJ, 925, 48
Yang, R.-z., Zhang, X., Yuan, Q., & Liu, S. 2014, A&A, 567, A23
Zhang, S., Tian, W., Zhang, M., et al. 2023, ApJ, 942, 94
Zhou, Y. 2017a, PhR, 720, 1
Zhou, Y. 2017b, PhR, 723, 1
Zweibel, E. G. 1979, in AIP Conf. Ser. 56, Particle Acceleration Mechanisms in Astrophysics, ed. J. Arons, C. McKee, & C. Max (Melville, NY: AIP), 319